Observations of Swirling Flows Behind Circular Disks

R. F. Huang* and F. C. Tsai†

National Taiwan University of Science and Technology, Taipei 10672, Taiwan, Republic of China

The flow patterns of a swirling jet subject to the influences of various central blockages are studied experimentally via the smoke-wire flow visualization method. Details of the observed flow structures are described and discussed. The flow structures display multiple modes, depending on the blockage ratio and swirl number. When the blockage ratio is less than about 0.1, swirling wake, vortex breakdown, and three-dimensional vortex shedding are observed for different ranges of swirl number. When the blockage ratio is greater than about 0.1, the bluff-body effect becomes significant. In this case, a pair of counter-rotating vortex rings and a central swirling jet characterize the flowfield. Axisymmetric vortex breakdown and three-dimensional vortex shedding may appear on the central swirling jet when the swirl number or blockage ratio is larger than critical values. Some characteristic quantities of the flowfield are measured and correlated, including the free separation lines, recirculation lengths, and frequencies of the vortex shedding.

Nomenclature

A	=	area at exit of swirling jet, $\pi(D_o^2 - D^2)/4$
B	=	blockage ratio, D^2/D_o^2
D	=	diameter of circular disk
D_h	=	hydraulic diameter of annular swirling jet at exit, $D_o - D$
D_m	=	mean diameter for calculating swirl number, $(D + D_o)/2$
D_o	=	outer diameter of annular swirling jet at exit
f	=	frequency of vortex shedding
L_r	=	recirculation length, measured from disk to maximum axial height of the recirculation bubble
L_{vb}	=	axial distance between vortex breakdown and circular disk
Q_a	=	volumetric flow rate
Re_a	=	Reynolds number, $u_a D_h / \nu$
r	=	radial coordinate, originated from center of circular disk
S	=	swirl number
Sr_D	=	Strouhal number of instabilities, $f D/u_a$
u	=	axial velocity component
u_a	=	volumetric mean axial velocity of annular swirling jet at exit, Q_a / A
v	=	radial velocity component
W_{max}	=	maximum width of contour of free separation line evolving from edge of disk
w	=	azimuthal velocity component
x	=	axial coordinate, originated from center of circular disk
ν	=	kinematic viscosity of air

Introduction

SWIRLING jets and bluff-body wakes have been widely used in many engineering applications, for example, industrial burners or gas turbine combustors. The fundamental idea of the application of the swirling jet or bluff-body wake is to benefit from the reverse flow in the near field, which causes the expedition of the mixing process. Many papers related to these two types of flows have been published during the past few decades.[1−9] Conventionally, nonswirling bluff-body wake and swirling jet were studied independently, because either the strong swirl intensity in the swirling jet or the large

*Professor, Department of Mechanical Engineering; rfhuang@mail.ntust.edu.tw. Member AIAA.

†Graduate Student, Department of Mechanical Engineering.

blockage itself in the nonswirling bluff-body wake could satisfy the expectations of flow reversal and mixing enhancement.

There has been little previous study of the combined effects of a swirling jet and a bluff body. Chigier and Beer[10] measured the velocity and static-pressure distributions in a swirling air jet that goes across a small centerbody with a small blockage ratio of 0.056. A time-averaged open-top toroidal flow structure in the near field with reversed flows along the central axis was recognized. Baker et al.[11] measured three velocity components in a furnace model with a small central hub of small blockage ratio 0.05. Both the nonswirling and swirling flows were studied. The results indicate that the swirling flow has a substantial region of recirculation on the axis in contrast to the nonswirling flow. Escudier and Keller[12] employed a confined swirling flow to go across a large cylindrical centerbody with blockage ratios 0.25 and 0.39 to justify Benjamin's theory[13] of vortex breakdown phenomena. Two reversed flow regions were observed: a recirculation bubble behind the cylindrical centerbody and an isolated axisymmetric recirculation zone (vortex breakdown) on the axis in the downstream section of the outer confining tube. As the swirl increases, the vortex breakdown moves upstream in the vortex tube. At a critical swirl strength, the recirculation bubble downstream of the central cylinder joins with the vortex breakdown and forms a single recirculation zone. The flow downstream of the recirculation zone becomes highly turbulent.

Sheen et al.[14] studied the structures of the recirculation zones of both unconfined and confined swirling jets with a centerbody of blockage ratio 0.23. Several characteristic flow regimes were identified at different swirl strengths. The flows in the transition regime present an unsteady asymmetric recirculation bubble. In the prepenetration regime, the recirculation bubble displays a stable two-celled structure with a stagnation point on the central axis. In the penetration regime, the fluids along the central axis penetrate the apex of the recirculation bubble. They also found that the primary physical phenomena of the characteristic flow modes exist at either low or high Reynolds numbers. At Reynolds numbers greater than 1×10^3, the critical swirl numbers do not change essentially. At Reynolds numbers lower than about 1×10^3, the values of the swirl numbers categorizing the flow modes go a little higher.

In general, a swirl number larger than 0.6 and a Reynolds number greater than 1.8×10^4 are required to induce a recirculation bubble in the near field of a swirling jet.[1] In the bluff-body wake, a large central blockage would induce a large pressure drop at large Reynolds numbers.[2] At low Reynolds numbers and small blockages, the recirculation intensity is usually not strong enough to cause beneficial applications. The study of the combined effects of the bluff body and swirling jet may provide insight into the physical phenomena and offer some ways to extend the applicability of swirling jet. In this paper, the behavior and flow patterns of a swirling jet at various swirl numbers and exit blockage ratios are studied with the laser-light sheet assisted smoke-wire flow visualization method. The

contributions are twofold. First, the blockage ratios cover a broad range, from 0.0256 to 0.5625, so that the physical phenomena and effects of the central blockage on the flowfields of the swirl jets are systematically manifested. Second, although the present results are at low Reynolds numbers, they may provide some insight into the flow behavior at higher Reynolds numbers.

Experimental Arrangement

Apparatus

The experiments are performed with the setup shown in Fig. 1. The airflow passes sequentially through the plenum chamber, flow conditioners, and curved settling chamber and is eventually deflected by the guide vanes. The flow conditioners consist of one set of honeycombs and three layers of wire-mesh screens. The honeycombs have a cell size of 3 mm and a length of 30 mm. The mesh size of the screens is 0.508 mm. An azimuthal component of velocity is imparted to the flow by the axisymmetric array of 12 guide vanes arranged on a pitch circle of radius 175 mm. The guide vanes are profiled in a NACA 0012 wing section with a chord length of 60 mm and a span of 50 mm. The vane angles can be adjusted from 0 to 70 deg with a resolution of 0.5 deg. A well-contoured nozzle with a contraction ratio of 9.0 is used to accelerate the flow and to decrease the turbulence intensity. A cylindrical test section with a diameter $D_o = 40$ mm is attached to the exit of the nozzle. The circular disk is placed at the center of the exit of the cylindrical test section. Several disks with diameters $D = 6.4, 8, 9, 10, 11, 12, 13, 14, 16, 20, 25,$ and 30 mm are employed in the experiments to make the blockage ratios, $B = (D/D_o)^2$, range from 0.0256 to 0.5625. The thickness of the disks is 1.4 mm in all cases.

The airflow is supplied with a ring blower. Before being fed into the test rig shown in Fig. 1, the airflow from the blower passes through a flow conditioning system, which consists of acoustical filters, pressure regulators, needle valves, rotameters, and particle seeding chambers. The acoustical filters incorporated into the system are required to suppress the fluctuations of velocity in the flow from the blower. The pressure regulator and the needle valve serve as the pressure stabilizer and flow rate controller, respectively. The flow rate is measured with several calibrated rotameters.

Flow Visualization Technique

A corrugated tungsten wire with a diameter of 200 μm is placed on the symmetry plane across the jet exit at a downstream distance of $x = 1$ mm. Thin mineral oil is brush coated on the wire surface and ohmically heated to generate fine smoke streaks to make the flowfield observable. The smoke streaks are about 0.7 mm in width, and the space between each smoke streak is controlled to within

Fig. 1   Experimental setup.

0.3 mm via the corrugation density of the wire. The observable smoke streaks generated by this configuration at $Re_a = 220$ can last for at least 90 s. The Reynolds number based on the smoke-wire diameter in this study is kept below 30, which is lower than the limit 40 recommended by Mueller[15] to avoid vortex shedding behind the wire. The surface temperature of the smoke wire is kept as low as possible, but still high enough to evaporate the oil so that the buoyancy-induced convection[16] is estimated to be below 2.5 cm/s. The diameter of the condensed vapor aerosols (the smoke) of the thin mineral oil measured by a Malvern 1600C Particle Analyzer is 1.7 ± 0.3 μm. The slip factor[17] of these aerosols is about 1.16. The stokes number[17] based on the diameter of the circular disk is approximately 0.001, which is much smaller than unity. In this case, the smoke streaks are expected to follow the flow properly. The two-dimensional flow patterns are observed by illuminating the flowfield with a laser-light sheet on the symmetry plane. Streak images are taken by a charge-coupled device (CCD) camera and recorded on the video tapes. Three-dimensional motions of the smoke streaks are visualized by illuminating the flowfield with a 500-W xenon lamp. Analysis is made based on both the visualized three-dimensional motions of smoke streaks and two-dimensional images recorded on the video tapes.

Detection of Instability Frequencies

A one-component hot-wire anemometer is used to measure the instability frequencies in the flowfield. To properly detect the frequency of the wake instabilities, the probe is positioned at $x = 3D$ and $0 < r < 0.5D$ to record the oscillations caused by the instabilities in the flow. The hot-wire probe is made of a platinum wire, 5 μm in diameter and 1.5 mm in length. The frequency response is electrically adjusted to about 20,000 Hz. The output signals of the hot-wire anemometer are conditioned with a resistance–capacitance (RC) filter before connecting to a fast Fourier transform (FFT) analyzer. The cutoff frequency of the filter is set to 6000 Hz.

Initial Conditions

The axial and tangential exit velocity profiles across $x/D_o = 0.1$ plane are measured with a two-component laser Doppler velocimeter (LDV). The dimensions of measuring volumes of the green and blue components are $0.075 \times 0.075 \times 0.680$ mm and $0.071 \times 0.071 \times 0.645$ mm, respectively. The fringe separations of green and blue components are 2.34 and 2.22 μm, respectively. The system is configured for forward scattering with a receiving angle of 10 deg off the central axis. Two counter processors are used to capture the Doppler signals. For LDV measurements, MgO particles with an average diameter of 1 μm are seeded into the annular flows by using a homemade fluidized bed. The seeding particles can respond up to 9 kHz according to Hjelmfelt and Mockros.[18] The digital outputs of the counter processors are fed into a data acquisition system. Each velocity data record consists of 3000 samples, about 0.3 s long. The average sampling rate is about 10 kHz.

The radial distributions of normalized exit axial and tangential velocities at $B = 0.5625$ for flows at various swirl numbers and Reynolds numbers are shown in Fig. 2. Each velocity profile is normalized by the maximum value for that profile. Similarities are observed for both axial and tangential velocities within experimental uncertainty. The influences induced by nonsimilar exit swirl profiles are thus avoided.[19] Both the peak values of axial and azimuthal velocity components appear at $r/D_o \approx 0.44$.

In the range of this study, the axial and tangential turbulence intensities at the exit measured by LDV are lower than 4.8 and 3.7%, respectively. However, they are lower than 1.4 and 1.1%, respectively, by using a hot-wire anemometer.

Determination of Swirl Number

The degree of swirl for a swirling flow is characterized by the swirl number S, which has been employed by many investigators.[1,8] It is basically a ratio of the axial flux of angular momentum to the axial flux of axial momentum:

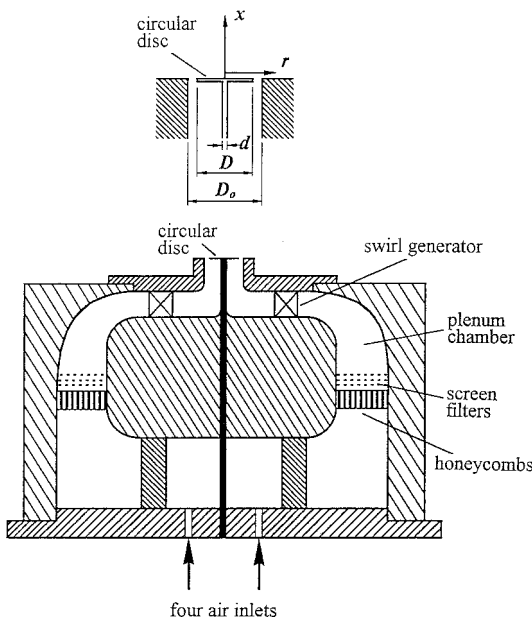$$S = \frac{\int_{D/2}^{D_o/2} uw r^2 \, dr}{(D_m/2)\int_{D/2}^{D_o/2} u^2 r \, dr} \qquad (1)$$

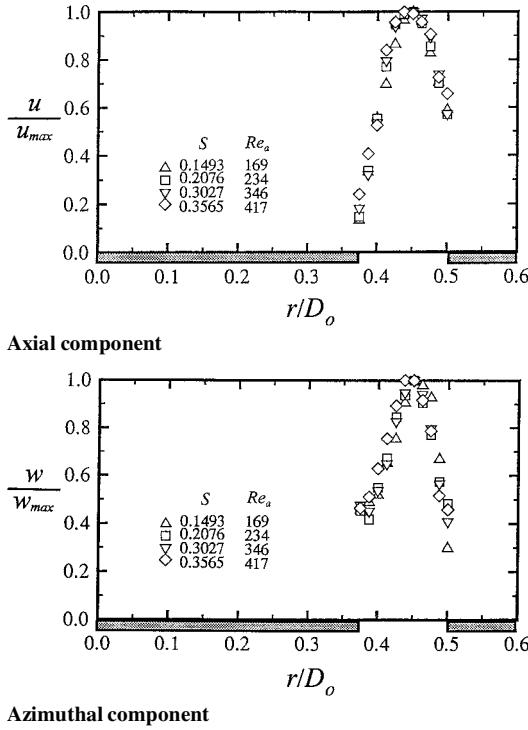**Axial component**

Azimuthal component

Fig. 2   Normalized exit velocity profile: data measured with a LDV system at $x/D_o = 0.1$.

The swirl numbers in this experiment are obtained by applying the measured velocity components u and w to Eq. (1).

Measurement Uncertainties

The rotameters used to measure the flow rate are calibrated in the laboratory with a microflow calibration system. The accuracy is $\pm 1\%$ of full scale. The uncertainty of the exit velocity measured by LDV is estimated to be less than $\pm 1.5\%$. Accuracy of the characteristic lengths of flow structures measured from the smoke-streak photographs is within $\pm 3\%$ of the disk diameter. The accuracy of the frequency measurement depends not only on the response of hot-wire anemometer but also on the record length and sampling rate of the FFT analyzer. The uncertainty of the frequency detection is estimated to be $\pm 0.75\%$.

Results and Discussion

Characteristic Flow Patterns

As shown in Fig. 3, depending on the blockage ratio B and swirl number S, several types of flow patterns are identified in different regimes: swirling-jet-dominated, weak-blockage-effect, and bluff-body-effect-dominated regimes. In determining the boundaries between different flow modes, the swirl number S is increased from small to large values at a given disk blockage B. The swirl number at which the flow pattern appears to change is recorded. Both visual observation and video images are used to identify the change of characteristic flow modes. A procedure of decreasing S is also conducted. No hysteresis effect is found. All 12 disks employed in this experiment are tested. Maximum ambiguity of the swirl number to identify boundaries between different flow modes is ± 0.01 about the recorded data.

Swirling-Jet-Dominated Regime

In the left lower corner of Fig. 3, no particular flow features are observed other than the ordinary flow phenomena of a weak swirling jet,[1,7,8] which is generally defined as $S < 0.6$ at $B = 0$. With such a low swirl number, neither recirculation bubble nor vortex breakdown[20] is found. Because the swirl-induced pressure decrease around the central line area of the jet is not large enough to overcome the axial momentum, no flow reversal occurs. The range of swirl number for this flow mode decreases when the blockage ratio is increased.
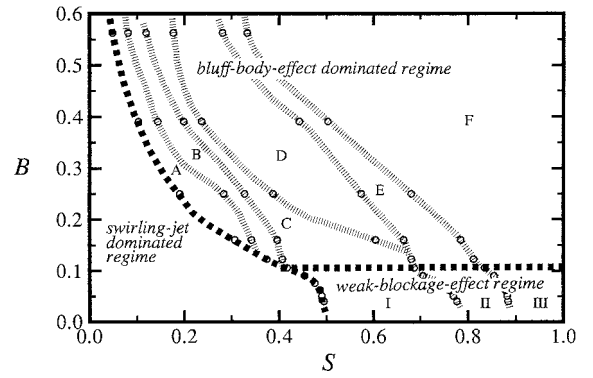

Fig. 3   Characteristic modes identified on the domain of blockage ratio and swirl number.
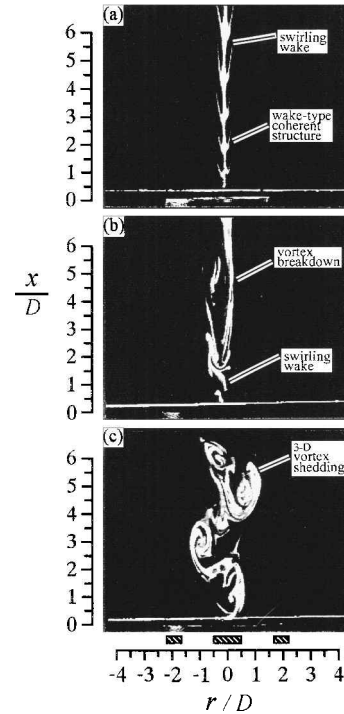

Fig. 4   Characteristic flow modes in weak-blockage-effect regime with $B = 0.09$ and shutter speed $= \frac{1}{100}$ s: a) mode I, swirling wake, $S = 0.6857$, and $Re_a = 358$; b) mode II, swirling wake with vortex breakdown, $S = 0.8033$, and $Re_a = 453$; and c) mode III, vortex shedding, $S = 0.8662$, and $Re_a = 515$.

Weak-Blockage-Effect Regime

In the weak-blockage-effect regime, the central disk causes some effects on the swirling jet that makes the flow features look different from those in the swirling-jet-dominated regime.

In mode I of the weak-blockage-effect regime, a swirling wake behind the disk is observed, as shown in Fig. 4a. Wake-type coherent structures appear on the shear layers. The smoke in the outer region surrounding the central swirling wake is dispersed and becomes invisible.

In mode II of the weak-blockage-effect regime, as the swirl increases an axisymmetric bubble-type vortex breakdown[21,22] appears in the downstream region of the central swirling wake, as shown in Fig. 4b. According to Gupta et al.,[1] the critical swirl number for forming a vortex breakdown in a swirling jet without a central blockage is about 0.6. In the present case of the weak-blockage-effect regime, where $B < 0.1$, the critical swirl number for the formation of a vortex breakdown is about 0.7–0.8. The critical value for the formation of a vortex breakdown decreases with the increase of blockage. Faler and Leibovich[23] have measured and described a two-celled structure in the bubble interior of the axisymmetric vortex breakdown induced in a swirling flow at a Reynolds number of 2.56×10^3 and a circulation number of 1.777. The image of the

inner cell can be seen around the base of the vortex breakdown, as shown in Fig. 4b. However, because the axisymmetric vortex breakdown in this case is a long bubble instead of a short one, which has been discussed in most of the literature,[10,20,23,24] the detailed structure inside the vortex breakdown is still unclear.

The axisymmetric vortex breakdown of mode II moves toward the upstream area with the further increase in swirl number. As the base of the vortex breakdown region almost touches the disk, the flow structure evolves to a three-dimensional vortex shedding, as shown in Fig. 4c. For the smallest disk employed in this study, that is, $B = 0.0265$, the vortex shedding does not appear. Instead, part of the vortex breakdown appears to move into the nozzle with the increase of swirl number. For the other 11 disks employed in this study, that is, $B \geq 0.04$, vortex shedding occurs in the regime of mode III. An approximate value of $B = 0.03$ may be acknowledged as a lower limit of blockage ratio for the evolution of vortex shedding. Many investigators[22,25,26] have presented time-averaged velocity measurements in a swirling jet or a combustor with a central blockage. At large swirl numbers, a reverse-flow region near the jet exit is typically observed. Whereas the dynamic motion of the vortex shedding observed in the present study may enhance the mixing effect in the downstream area, it may also cause an unsteady wave propagation in a combustor. This result may provide a physical reasoning for the Gupta et al. proposal[1] of using a small central hub in a combustor swirler to avoid low-frequency flow oscillation at large swirl numbers.

Bluff-Body-Effect-Dominated Regime

In the regime $B > 0.1$, the effect of central bluff body becomes important. Six characteristic flow modes are identified, as shown in Fig. 3.

Figure 5a shows the typical flow pattern of mode A in the bluff-body-effect-dominated regime. A Q-tip pattern is formed in the central part of the wake. Because no smoke streaks present in the Q tip, the central flow does not go downstream. The reversed flow along the centerline was revealed by introducing TiO_2 smoke into the Q-tip region with a fine metal wire. The flow is found to convect upstream, spread outward, then turn downstream. The Q-tip region, characterized by an axial flow reversal near the axis, resembles the meridional flow derived by Sullivan.[27] Sullivan's solution of a swirling flow near a wall illustrates that low pressure in the core region near the wall, which is induced by the rotating flow motion, can cause reversal of the axial flow.

In mode B of the bluff-body-effect-dominated regime, as the swirl strength increases, the flow pattern becomes an open-top toroid, as shown in Fig. 5b. Because of the increase of the pressure gradient induced by the swirl motion of fluids and bluff-body effect, the vorticity in the head area of the Q tip is increased.[28] The vortical motion entrains smoke from outer smoke streaks so that the vortex in the central toroid is clearly seen. The central reverse flow still exists that shows no smoke streaks. The free separation lines extend to far downstream without returning to the vorticity-concentrated region. Some secondary vortices are observed between the central vortex region and the free separation lines.

In mode C of the bluff-body-effect-dominated regime, an additional recirculation bubble is observed. The separation lines evolving from the edge of the circular disk turn back and form an outer vortex ring, as shown in Fig. 5c. The flow structure in the center core appears to be quite unsteady. The rotating and tumbling motions of large eddies are observed. The fluids in the center core are eventually expelled downstream in a central rotating fluid column, which looks like a swirling jet issuing from the recirculating flow region. The rotation of the central fluid column has the same direction as the annular swirling flow. Surrounding the center core are annular swirling flows. They are invisible because the smoke streaks rotate off the plane of the laser-light sheet.

For yet higher swirl strength, in mode D of the bluff-body-effect-dominated regime, the strength of the rotating motion in the outer vortex ring is enhanced, and the unsteady motions in the center core are stabilized. A central swirling jet emerging from the disk surface is surrounded by an inner vortex ring, as shown in Fig. 6a. The inner and outer vortex rings rotate in the opposite directions. Jet-type coherent structures along the shear layer of the swirling central jet are observed. Figure 6d shows the speculative topologically correct flow pattern for the near-wake bubble. The coherent structures along the shear layer of the central swirling jet are ignored so that the large structures in the near-wake bubble are prominently presented. Figures 6d–6f are determined by both the smoke-streak
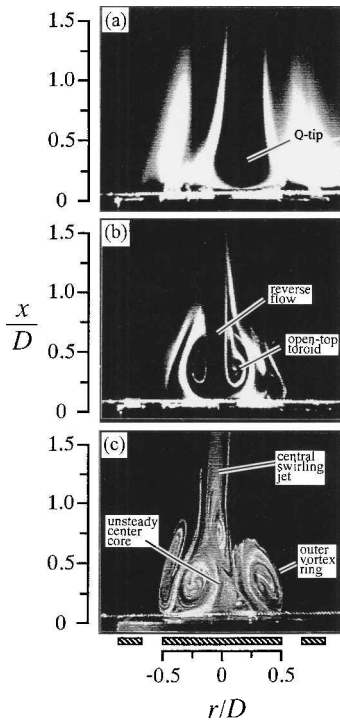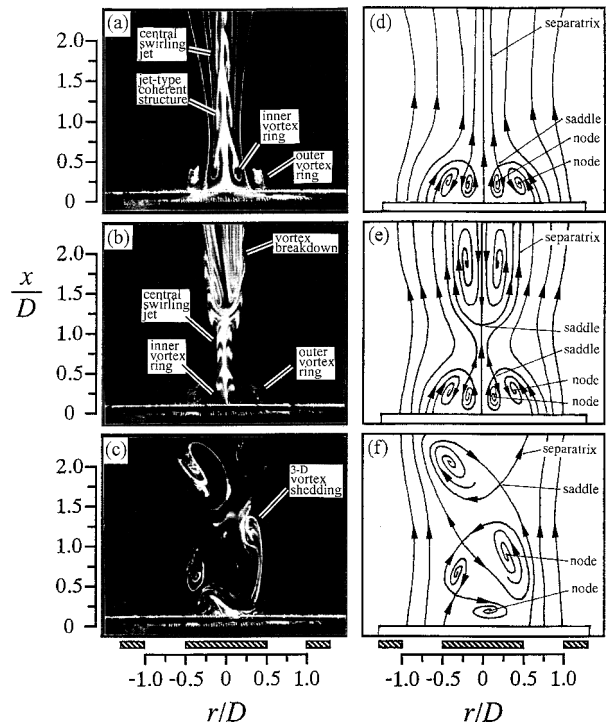

Fig. 5 Characteristic flow modes in bluff-body-effect dominated regime with $B = 0.5625$, shutter speed $= \frac{1}{100}$ s: a) mode A, $S = 0.0689$, and $Re_a = 91$; b) mode B, $S = 0.0855$, and $Re_a = 99$; and c) mode C, $S = 0.1644$, and $Re_a = 186$.

Fig. 6 Characteristic flow modes in bluff-body-effect dominated regime with $B = 0.25$ and shutter speed $= \frac{1}{100}$ s: a) photograph, mode D, $S = 0.4638$, and $Re_a = 255$; b) photograph, mode E, $S = 0.6408$, and $Re_a = 393$; c) photograph, mode F, $S = 0.6983$, and $Re_a = 446$; d) topological flow pattern, conditions of part a; e) topological flow pattern, conditions of part b; and f) topological flow pattern; conditions of part c.

images and motion pictures. Following Perry and Fairlie,[29] as well as Chong and Perry,[30] the speculative topological flow pattern is characterized by critical points, separatrices, and alleyways.[29,30] In the topology terminology, a critical point is a point in a flowfield where the streamline slope is indeterminate, a separatrix is a streamline leaving or terminating at a saddle, and an alleyway is a passageway in between the two separatrices. In the present case, the critical points consist of saddles and nodes. Topologically, the focus and center all belong to nodes. A saddle point must exist between the outer and inner vortex rings to satisfy the topological rules. From the topological point of view, the flow reversal in the outer vortex ring causes the inner vortex ring to form, which in turn establishes the central swirling jet. Through visual observation, the rotation speed in the central rotating jet increases with the increase of swirl number.

In mode E of the bluff-body-effect-dominated regime, the inner vortex rings and the central jet rotate faster than those of mode D. A vortex breakdown[21,22] similar to the flow pattern of mode II in the weak-blockage-effect regime is formed in the downstream area of the swirling central jet, as shown in Figs. 6b and 6e. Again, the jet-type coherent structures are ignored in Fig. 6e. Only the speculative topologically correct flow pattern for the near-wake bubble and vortex breakdown is shown. There is a stagnation point (which is a saddle) that appears at the bottom of the vortex breakdown. The vortex breakdown moves upstream with the increase of swirl number.

In mode F of the bluff-body-effect-dominated regime, the vortex breakdown touches the circular disk, and the flow structure becomes

unsteady. Three-dimensional vortices are shed periodically in the wake, as shown in Fig. 6c. The speculative topologically correct flow pattern is shown in Fig. 6f. The vortex shedding is similar to that of mode III in the weak-blockage-effect regime. A stable instantaneous recirculation zone is never found in this flow mode.

Characteristic Lengths

The data for the separation line and recirculation length were measured by averaging 30 flow visualization images recorded on the video tapes. They are magnified 10 times to reduce the measurement error.
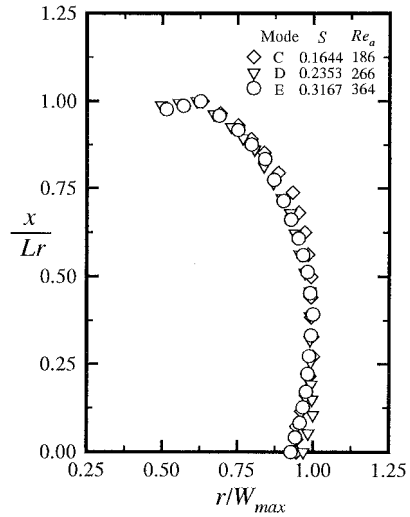
Separation Lines

The normalized free separation lines evolving from the edge of the circular disk in the bluff-body-effect-dominated regime at various swirl numbers and Reynolds numbers are shown in Fig. 7a. In modes A and B, the separation lines first expand slightly outward from the edge of the disk, then curve inward, and finally evolve to the downstream area without any reversal. However, in modes C–E, where the swirl number is larger, the large pressure gradient built up around the near wake causes the separation lines to turn back and form an outer vortex ring. If the x and r coordinates of the separation lines of modes D–F are normalized by the recirculation length Lr and maximum width W_{max}, respectively, the scattered data of Fig. 7a become well correlated, as shown in Fig. 7b.

Recirculation Length

The variation of the normalized recirculation length of the outer vortex ring in modes C–F of the bluff-body-effect-dominated regime with S at various blockage ratios is shown in Fig. 8a. At all blockage ratios, the normalized recirculation length increases almost linearly with the increase of swirl number in mode C. It attains maximum value and starts to shorten in mode D. In mode E, Lr/D decreases gradually with the increase of swirl number. Figure 8b shows comparisons of the bubble length between the nonswirling wake and the swirling wake. Present measurements of the nonswirling wake correlate well with Li and Tankin's data.[5] Apparently, the swirl
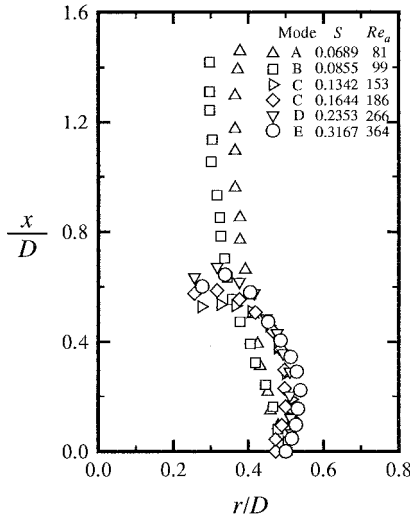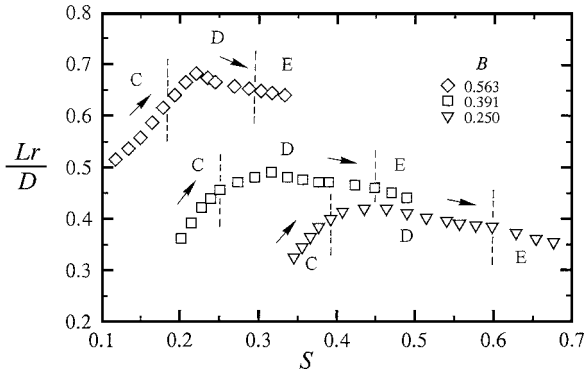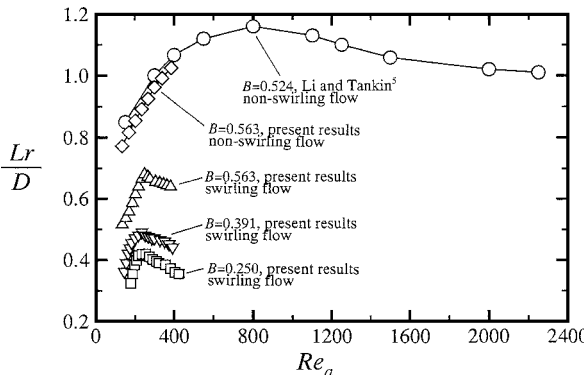

a) Normalized by disk diameter

b) Normalized by Lr and W_{max}

Fig. 7   Free separation lines in bluff-body-effect dominated regime.

a) Variations with swirl number

b) Comparison with nonswirling bluff-body wake

Fig. 8   Recirculation length of outer vortex ring of swirling wakes in bluff-body-effect dominated regime.
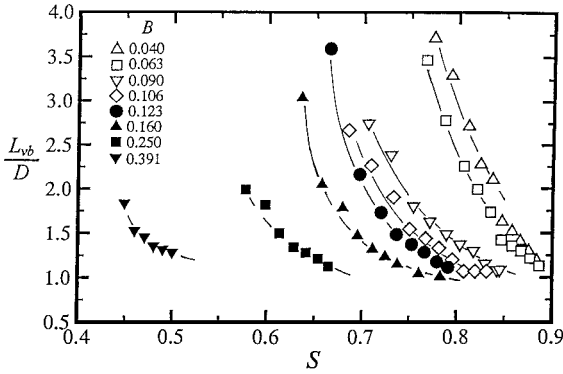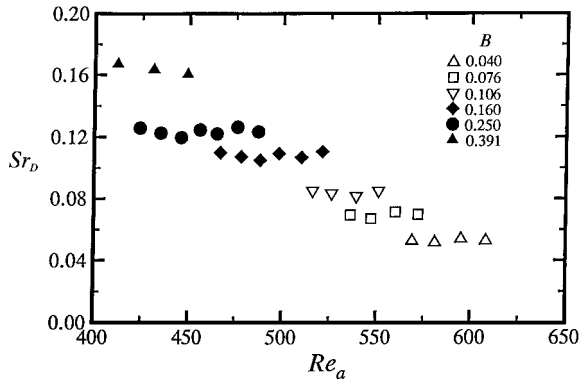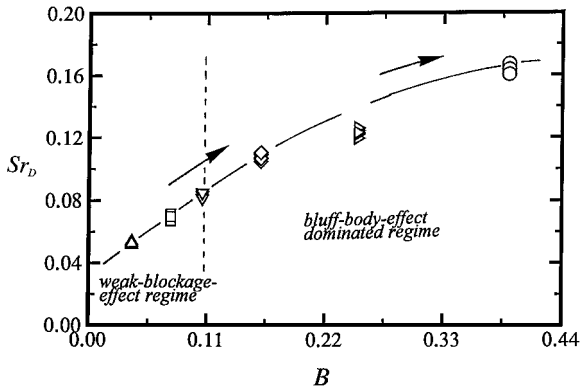
Fig. 9 Axial length of vortex breakdown in modes II and E.

a) Variation with Reynolds number

b) Effects of blockage ratio

Fig. 10 Strouhal number of vortex shedding after attachment of vortex breakdown to the circular disk in modes III and F.

imparted to the annular flows significantly shortens the recirculation length.

Axial Distance of Vortex Breakdown

Figure 9 shows the variation of the normalized axial distance between the base of the vortex breakdown region and the circular disk. The vortex breakdown takes place in both mode II of the weak-blockage-effect regime and mode E of the bluff-body-dominated regime. At all blockage ratios, L_{vb}/D decreases nonlinearly with the increase of S. A vortex breakdown can be maintained at an axial level with either a larger S at a small B or a smaller S at a large B. In other words, the local swirl strength in the central swirling jet is enhanced as either S or B is increased. The increase of the rotation speed in the central swirling jet can be observed during the experiments, when the swirl number or the blockage ratio is increased.

Frequency of Vortex Shedding

Three-dimensional vortex shedding is observed in both mode III of the weak-blockage-effect regime and mode F of the bluff-

body-effect-dominated regime. Although the planar images shown in Figs. 4c and 6c do not ascertain the three-dimensional characteristics, the meandering of the initial planar streaks from the smoke wire do show the rotating motion around the central axis. By the proper placement of a hot-wire anemometer probe in the disk wake, the shedding frequencies of the vortices are detected as low as 1.5 Hz. Figure 10a presents the variation of the nondimensional frequency and the Strouhal number Sr_D with the Reynolds number Re_a at various blockage ratios. The Strouhal number at constant blockage ratio does not change significantly with Reynolds number. However, Strouhal number Sr_D increases with the increase of blockage ratio, as shown in Fig. 10b. In the weak-blockage-effect regime, the increase rate is almost linear. However, the increase rate of the Strouhal number decreases in the bluff-body-effect regime and may approach around 0.165 at large blockage ratios, which is comparable to the value $1/2\pi (= 0.159)$ predicted by the universal Strouhal law derived by Levi.[31]

Conclusions

The flow patterns induced by the combined effects of swirling jet and central blockage have been studied via the smoke-wire flow visualization method. Depending on the blockage ratio and degree of swirl, three characteristic regimes are identified, which are swirling-jet, weak-blockage-effect, and bluff-body-effect regimes. In the swirling-jet regime, the flows behave similarly to a ordinary swirling jet. In the weak-blockage-effect regime, the central blockage causes slight effects on the swirling flow so that a swirling wake is formed. In the bluff-body-effect regime, the blockage induces a complicated dual-ring bubble structure standing behind the disk. There are several modes further identified in the weak-blockage-effect and bluff-body-effect regimes.

In the bluff-body-effect regime, six specific flow modes are identified. The flowfields of modes C and D are characterized by a pair of counter-rotating vortex rings and a central swirling jet. The dual-ring recirculation bubbles can be formed at low swirl numbers even if the Reynolds numbers are low. Therefore, in practical applications, by installing a proper central blockage and operating the swirling jet in the bluff-body-effect regime, the swirl and Reynolds required for forming the recirculation bubble in the near field can be lowered drastically.

References

[1]Gupta, A. K., Lilley, D. G., and Syred, N., *Swirl Flows*, Abacus, Cambridge, MA, 1984, pp. 13–117.
[2]Carmody, T., "Establishment of the Wake Behind a Disk," *Journal of Basic Engineering*, Vol. 86, Dec. 1964, pp. 869–882.
[3]Taylor, M. K. P., and Whitelaw, J. H., "Velocity Characteristics in the Turbulent Near Wakes of Confined Axisymmetric Bluff Bodies," *Journal of Fluid Mechanics*, Vol. 139, Feb. 1984, pp. 391–416.
[4]Schefer, R. W., Namazian, M., and Kelly, J., "Velocity Measurements in Turbulent Bluff-Body Stabilized Flows," *AIAA Journal*, Vol. 32, No. 9, 1994, pp. 1844–1851.
[5]Li, X., and Tankin, R. S., "A Study of Cold and Combusting Flow Around Bluff-Body Combustors," *Combustion Science and Technology*, Vol. 52, 1987, pp. 173–206.
[6]Huang, R. F., and Lin, C. L., "Visualized Flow Patterns of Double Concentric Jets at Low Annulus Velocities," *AIAA Journal*, Vol. 32, No. 9, 1994, pp. 1868–1874.
[7]Rose, W. G., "A Swirling Round Turbulent Jet 1—Mean-Flow Measurements," *Journal of Applied Mechanics*, Vol. 29, Dec. 1962, pp. 615–625.
[8]Chigier, N. A., and Chervinsky, A., "Experimental Investigation of Swirling Vortex Motions in Jets," *Journal of Applied Mechanics*, Vol. 89, June 1967, pp. 443–451.
[9]Kerr, N. M., and Fraser, D., "Swirl. Part 1: Effect on Axisymmetrical Turbulent Jets," *Journal of the Institute of Fuel.*, Vol. 38, 1965, pp. 519–526.
[10]Chigier, N. A., and Beer, J. M., "Velocity and Static Pressure Distributions in Swirling Air Jets Issuing from Annular and Divergent Nozzles," *Transactions of the American Society of Mechanical Engineers*, Ser. D, Vol. 86, Dec. 1964, pp. 788–798.

[11]Baker, R. J., Hutchinson, P., Khallil, E. E., and Whitelaw, J. H., "Measurements of Three Velocity Components in a Model Furnace with and without Combustion," *Fifteenth Symposium (International) on Combustion*, Combustion Inst., Pittsburgh, PA, 1974, pp. 553–559.

[12]Escudier, M. P., and Keller, J. J., "Recirculation in Swirling Flow: A Manifestation of Vortex Breakdown," *AIAA Journal*, Vol. 23, No. 1, 1985, pp. 111–116.

[13]Benjamin, B., "Theory of Vortex Breakdown Phenomena," *Journal of Fluid Mechanics*, Vol. 14, 1962, pp. 593–629.

[14]Sheen, H. J., Chen, W. J., and Jeng, S. Y., "Recirculation Zones of Unconfined and Confined Annular Swirling Jets," *AIAA Journal*, Vol. 34, No. 3, 1996, pp. 572–579.

[15]Mueller, T. J., "Flow Visualization by Direct Injection," *Fluid Mechanics Measurements*, 2nd ed., edited by R. J. Goldstein, Taylor and Francis, Washington, DC, 1996, pp. 367–450.

[16]Bejan, A., *Convective Heat Transfer*, Wiley, New York, 1984, pp. 110–114.

[17]Flagan, R. C., and Seinfeld, J. H., *Fundamentals of Air Pollution Engineering*, Prentice–Hall, Englewood Cliffs, NJ, 1988, pp. 295–307.

[18]Hjelmfelt, A. T., and Mockros, L. F., "Motion of Discrete Particles in a Turbulent Fluid," *Applied Scientific Research*, Vol. 16, 1966, pp. 149–154.

[19]Farokhi, S., and Taghavi, R., "Effect of Initial Swirl Distribution on the Evolution of a Turbulent Jet," *AIAA Journal*, Vol. 27, No. 6, 1989, pp. 700–706.

[20]Leibovich, S., "Vortex Stability and Breakdown: Survey and Extension," *AIAA Journal*, Vol. 22, No. 9, 1983, pp. 1192–1206.

[21]Harvey, J. K., "Some Observation of the Vortex Breakdown Phenomenon," *Journal of Fluid Mechanics*, Vol. 14, Pt. 4, 1962, pp. 585–592.

[22]Sarpkaya, T., "On Stationary and Traveling Vortex Breakdown," *Journal of Fluid Mechanics*, Vol. 45, Pt. 3, 1971, pp. 545–559.

[23]Faler, J. H., and Leibovich, S., "An Experimental Map of the Internal Structure of a Vortex Breakdown," *Journal of Fluid Mechanics*, Vol. 86, Pt. 2, 1978, pp. 313–335.

[24]Sloan, D. G., Smith, P. J., and Smoot, L. D., "Modeling of Swirl in Turbulent Flow Systems," *Progress in Energy and Combustion Science*, Vol. 12, 1986, pp. 163–250.

[25]Habib, M. A., and Whitelaw, J. H., "Velocity Characteristics of Confined Coaxial Jets With and Without Swirl," *Journal of Fluids Engineering*, Vol. 102, March 1980, pp. 47–53.

[26]Vu, B. T., and Gouldin, C., "Flow Measurements in a Model Swirl Combustor," *AIAA Journal*, Vol. 20, No. 5, 1982, pp. 642–651.

[27]Sullivan, R. D., "A Two-Cell Vortex Solution of the Navier–Stokes Equations," *Journal of the Aeronautical Sciences*, Vol. 26, No. 11, 1959, pp. 767–780.

[28]Lugt, H. J., *Vortex Flow in Nature and Technology*, Wiley, New York, 1983, pp. 253, 254.

[29]Perry, A. E., and Fairlie, B. D., "Critical Points in Flow Patterns," *Advances in Geophysics*, Vol. 18, No. B, 1974, pp. 299–315.

[30]Chong, M. S., and Perry, A. E., "A General Classification of Three-Dimensional Flow Fields," *Physics of Fluids A*, Vol. 2, No. 5, 1990, pp. 765–777.

[31]Levi, E., "A Universal Strhoul Law," *Journal of Engineering Mechanics*, Vol. 109, 1983, pp. 718–727.

J. C. Hermanson
Associate Editor